



# An allosteric propofol-binding site in kinesin disrupts kinesin-mediated processive movement on microtubules

Received for publication, January 30, 2018, and in revised form, May 24, 2018. Published, Papers in Press, May 29, 2018, DOI 10.1074/jbc.RA118.002182

Kellie A. Woll<sup>‡</sup>, Stephanie Guzik-Lendrum<sup>§</sup>, Brandon M. Bense<sup>§</sup>, Natarajan V. Bhanu<sup>¶</sup>, William P. Dailey<sup>||</sup>, Benjamin A. Garcia<sup>¶</sup>, Susan P. Gilbert<sup>§</sup>, and Roderic G. Eckenhoff<sup>‡1</sup>

From the <sup>‡</sup>Department of Anesthesiology and Critical Care and the <sup>¶</sup>Department of Biochemistry and Biophysics, Epigenetics Program, University of Pennsylvania, Perelman School of Medicine, Philadelphia, Pennsylvania 19104, the <sup>§</sup>Department of Biological Sciences and the Center for Biotechnology and Interdisciplinary Studies, Rensselaer Polytechnic Institute, Troy, New York 12180, and the <sup>||</sup>Department of Chemistry, University of Pennsylvania School of Arts and Sciences, Philadelphia, Pennsylvania 19104

Edited by Velia M. Fowler

Microtubule-based molecular motors mediate transport of intracellular cargo to subdomains in neurons. Previous evidence has suggested that the anesthetic propofol decreases the average run-length potential of the major anterograde transporters kinesin-1 and kinesin-2 without altering their velocity. This effect on kinesin has not been observed with other inhibitors, stimulating considerable interest in the underlying mechanism. Here, we used a photoactive derivative of propofol, *meta*-azipropofol (AziPm), to search for potential propofol-binding sites in kinesin. Single-molecule motility assays confirmed that AziPm and propofol similarly inhibit kinesin-1 and kinesin-2. We then applied AziPm in semiquantitative radiolabeling and MS microsequencing assays to identify propofol-binding sites within microtubule–kinesin complexes. The radiolabeling experiments suggested preferential AziPm binding to the ATP-bound microtubule–kinesin complex. The photolabeled residues were contained within the kinesin motor domain rather than at the motor domain– $\beta$ -tubulin interface. No residues within the P-loop of kinesin were photolabeled, indicating an inhibitory mechanism that does not directly affect ATPase activity and has an effect on run length without changing velocity. Our results also indicated that when the kinesin motor interacts with the microtubule during its processive run, a site forms in kinesin to which propofol can then bind and allosterically disrupt the kinesin–microtubule interaction, resulting in kinesin detachment and run termination. The discovery of the propofol-binding allosteric site in kinesin may improve our understanding of the strict coordination of the motor heads during the processive run. We hypothesize that propofol's potent effect on intracellular transport contributes to various components of its anesthetic action.

Neurons are highly polarized cells with numerous complex cellular subdomains, such as pre- and post-synaptic termini, which have specialized roles in electrochemical signaling. Because the biosynthetic and degradative machinery reside in the cell body, neurons are uniquely dependent on microtubule-based intracellular transport to deliver their vesicles, organelles, proteins, and RNA to synapses located a meter or more away (reviewed in Refs. 1–4). The human kinesin superfamily includes 45 genes, 38 of which are expressed in brain (5). Three subfamilies of kinesins are predominantly responsible for the fast ( $\sim 2$ – $5 \mu\text{m/s}$ ) (6, 7) and slow ( $\sim 0.02$ – $0.09 \mu\text{m/s}$ ) (8) transport of cargo to synapses. In contrast, cytoplasmic dynein is the major molecular motor responsible for retrograde transport to the cell body (2, 3, 9, 10).

The transport kinesins are dimeric with two catalytic motor domains dimerized through a coiled-coil stalk with globular C-terminal domains. The C-terminal domains interact with specific adaptors for cargo binding (reviewed in Refs. 2–4, 11, and 12)). Although conventional kinesin-1 (KIF5 in humans) is homodimeric (13, 14), kinesin-2 KIF3AB and KIF3AC are heterodimeric products of three genes, *KIF3A*, *KIF3B*, and *KIF3C* (15–19). The transport kinesins move along the microtubule in a precise manner in which each ATP turnover is coupled to an 8-nm step, the distance between adjacent  $\alpha\beta$ -tubulin dimers along the microtubule lattice (20–22). Remarkably, kinesin can complete one hundred steps or more in an asymmetric hand-over-hand manner, and therefore is referred to as “processive” (23–25). The ATPase cycles of each kinesin head must be coordinated and remain out-of-phase with each other to continue a processive run. If both heads reach a microtubule weak binding state at the same time, the processive run ends, and the motor with its cargo detaches from the microtubule (Fig. 1).

Previously, we reported that the commonly administered general anesthetic propofol (Fig. 2A) at clinically relevant concentrations inhibits the processive movement of kinesin-1 KIF5B and kinesin-2 KIF3AB and KIF3AC (26). The single molecule results showed that the average distance these kinesins could step decreased 40–60% with  $EC_{50}$  values  $<100 \text{ nM}$  propofol with no effect on the velocity of movement. These results indicate that propofol is not binding at the ATP-binding site or allosteric sites that modulate microtubule-activated ATP turnover. Rather, the results suggest that during a processive step on the microtubule, an allosteric binding site for

This work was supported in part by National Institutes of Health Grants R37-GM054141 (to S. P. G.), P01-GM55876 (to R. G. E.), and GM110174 and A1118891 (to B. A. G.), and National Science Foundation Graduate Research Fellowship Program Grant DGE-1321851 (to K. A. W.). The authors declare that they have no conflicts of interest with the contents of this article. The content is solely the responsibility of the authors and does not necessarily represent the official views of the National Institutes of Health.

✂ Author's Choice—Final version open access under the terms of the Creative Commons CC-BY license.

This article contains Figs. S1–S14 and Tables S1 and S2.

<sup>1</sup> To whom correspondence should be addressed: 3620 Hamilton Walk, Philadelphia, PA 19104-6112. Tel.: 215-662-3705; Fax: 215-349-5078; E-mail: roderic.eckenhoff@uphs.upenn.edu.

## Identification of inhibitory propofol site within kinesins

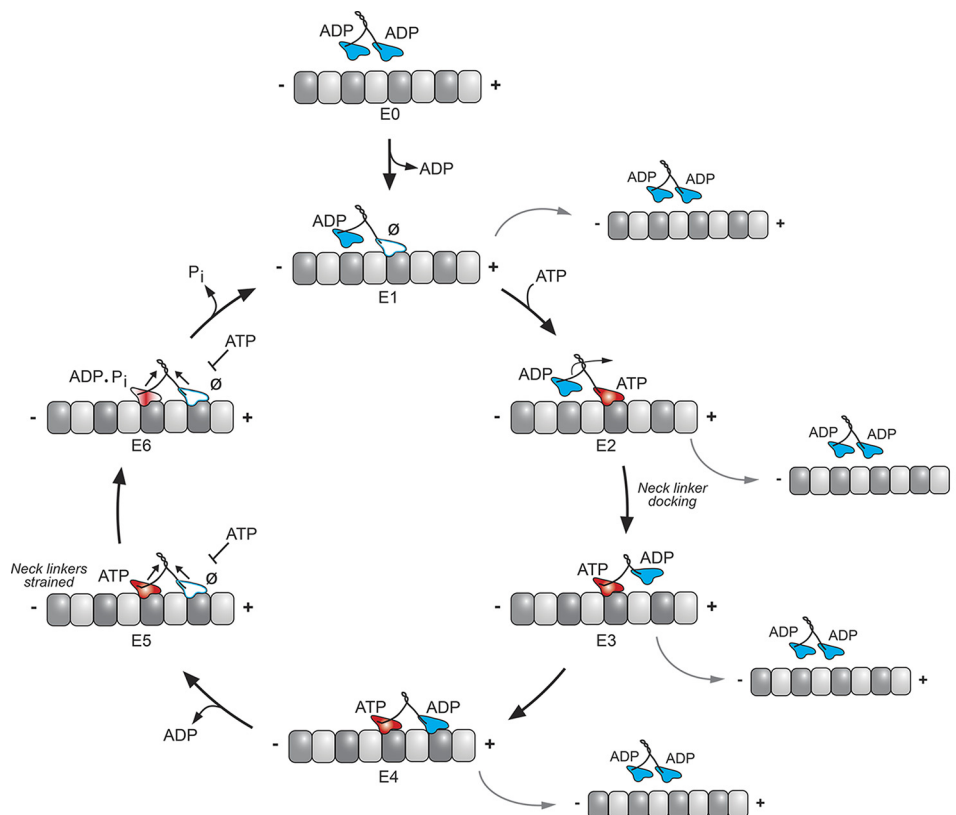


**Figure 1. Generalized schematic of the kinesin stepping cycle with proposed states for propofol-induced premature detachment from the microtubule.** *E0*, dimeric kinesin in solution, detached from the microtubule holds ADP tightly bound in each motor head. *E0–E1*, the processive run starts with microtubule collision followed by ADP release. The leading head is in the no-nucleotide state (white; Ø) and the trailing head is detached from the microtubule with ADP tightly bound. *E2–E4*, ATP binding at the leading head initiates a series of structural transitions, namely the ridged movement of the P-loop and Switch I/II motor head subdomains and neck linker docking that promotes the trailing head to move forward to the next microtubule-binding site. *E4–E5*, ADP is released from the leading head resulting in a two-head bound state. Strain develops, the leading head neck linker is detached and pointed backward, which decreases the probability of ATP binding to the leading nucleotide-free head. *E5–E1*, ATP hydrolysis within the trailing head followed by  $P_i$  release weakens the affinity of the trailing head to the microtubule, resulting in its subsequent detachment. The leading head is now able to bind another ATP to continue the processive run. The states most vulnerable to propofol-induced detachment from the microtubule include *E1–E4* based on the AziPm photolabeling.

propofol forms, propofol binds and disrupts the kinesin–microtubule interaction, and therefore results in kinesin detachment to end the processive run (26).

These results led us to hypothesize that propofol's effect on the neuronal transport kinesins may contribute to the multiplex nature of propofol induction and emergence (27) and/or adverse effects. Although an isolated processivity effect on some kinesins may not translate to large cellular or organism effects, the impact might be larger with prolonged exposures, such as in total intravenous administration (TIVA), ICU sedation, or in particularly sensitive brain regions and/or cell types.

To define the underlying molecular mechanism by which propofol ends a processive run, we pursued a study to identify propofol-binding site(s) on the microtubule–kinesin complex and determine their nucleotide-state dependence. The identification strategy used a photoactive analogue of propofol, *meta*-azi-propofol (AziPm)<sup>2</sup> (Fig. 2A), coupled with high-resolution

MS (28). The residues photolabeled by AziPm were located in the motor domains of kinesin-1 and kinesin-2 KIF3B and KIF3C. Interestingly no residues were photolabeled in the KIF3A polypeptide of heterodimeric KIF3AB or KIF3AC. Moreover, the shared allosteric site identified in each was distinct from the ATP-binding site at the conserved Switch I/II subdomain that is highly dynamic over the course of the kinesin stepping cycle (14, 29–33). These results identify a new drug-gable site in the kinesin family and provide insight into the potential effects of anesthetics on intracellular transport.

## Results

### Alkylphenol-based anesthetics selectively impair kinesin-1 and kinesin-2 run-length potential

We first sought to confirm that the photoaffinity derivative for propofol, AziPm, displayed activity analogous to the parent drug propofol. We employed a quantum-dot (Qdot) single molecule assay in conjunction with total internal reflection fluorescence (TIRF) microscopy to evaluate AziPm effects on processive kinesin motility (26). The single-molecule motility assay allows quantitative assessment of a motor's run length and velocity of movement by tracking single Qdot-bound kinesin dimers as they step along stationary microtubules (Fig. S1). We examined the effects of AziPm on the motility of a bacterially

<sup>2</sup>The abbreviations used are: AziPm, *meta*-azi-propofol; ACN, acetonitrile; AMPNP, adenosine 5'-( $\beta$ , $\gamma$ -imino)-triphosphate; ADP-AIF<sub>4</sub><sup>-</sup>, adenosine diphosphate-aluminum fluoride; CASTp, Computed Atlas of Surface Topography of proteins; GABA<sub>A</sub>,  $\gamma$ -aminobutyric acid type A; IPTG, isopropyl  $\beta$ -D-1-thiogalactopyranoside; LB, lysogeny broth; Qdot, quantum-dot; SHD, synthetic heterodimerization helix; TIVA, total intravenous administration; TIRF, total internal reflection fluorescence; TEV, tobacco etch virus.

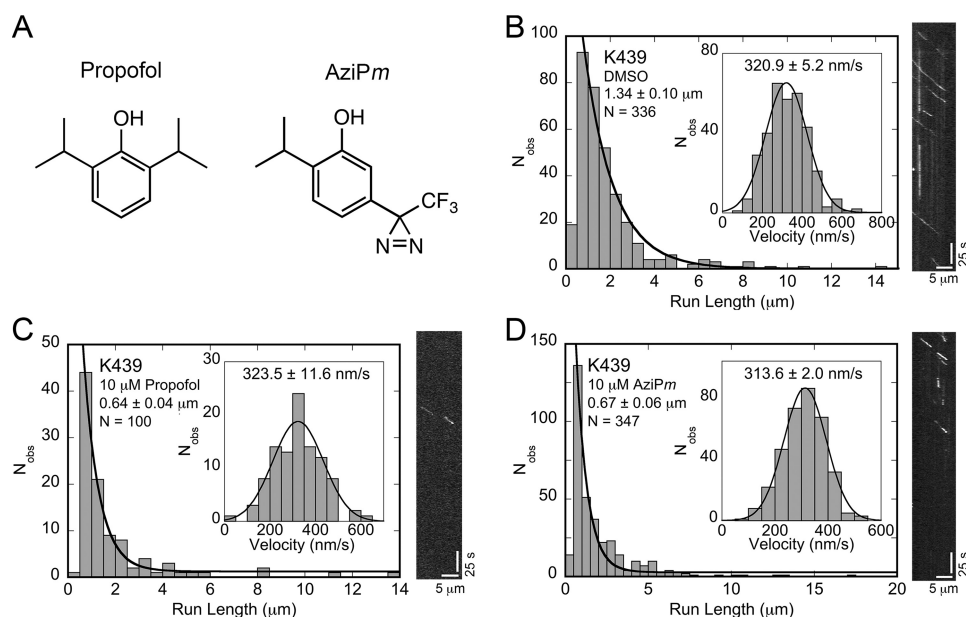


**Figure 2. AziPm-like propofol disrupts kinesin-1 processivity without an impact on velocity.** *A*, comparison of the chemical structure of propofol with its photoaffinity derivative, AziPm. *B–D*, single molecule K439 run length and velocity (*inset*) data and representative kymographs of Qdot-labeled K439 motors in (*B*) 5% DMSO control, (*C*) 10  $\mu$ M propofol, and (*D*) 10  $\mu$ M AziPm. A single exponential decay fit provides the mean run length  $\pm$  S.E. for each dataset. Mean run-length differences between the DMSO control and either propofol or AziPm were highly significant ( $p \ll 0.0001$ ), yet the mean run lengths of propofol and AziPm conditions showed no statistical significance from each other ( $p > 0.3$ ). A Gaussian fit provides the mean velocity  $\pm$  S.E. for each dataset, which were not statistically significant between the DMSO control and either propofol or AziPm ( $p > 0.1$ ). Kymograph scale bars: 5  $\mu$ m along the x axis, 25 s along the y axis.

expressed homodimeric conventional kinesin-1 (K439) that encodes the first 439 amino acid residues of human KIF5B. Homodimeric KIF5 motors have been identified as one of the primary motors for anterograde axonal transport of various cargos including vesicles and organelles such as mitochondria (2, 34). Both propofol and AziPm significantly decreased the run-length potential of K439 by  $\sim 50\%$  without altering motor velocity ( $p > 0.1$ ) (Fig. 2, *B–D*). This unique disruption in processivity aligned with our previous study where propofol decreased the distance traveled by the well-studied kinesin-1 motor K560 (26), contains the first 560 amino acid residues of KIF5B.

We then extended our study to determine whether AziPm, like propofol, also altered the processive movement of kinesin-2 motors. Heterodimeric KIF3 motors have been shown to be important for neurite building and the anterograde component for late endosomes/lysosome bidirectional axonal transport (35–37). Similar to propofol, AziPm decreased the run lengths of heterodimeric kinesin-2 KIF3AB and KIF3AC (Fig. S1). Previously we determined that propofol exhibited a level of selectivity for affecting kinesin-2 motors. Namely, propofol decreased the run length of engineered homomeric KIF3BB and KIF3CC but showed no effect on a similarly designed KIF3AA (26). AziPm displayed a similar selective inhibition of KIF3BB and KIF3CC motors at 10  $\mu$ M, decreasing their run lengths by  $\sim 50$  and  $\sim 35\%$ , respectively, whereas no significant change in the velocity of movement or the run length was observed for KIF3AA (Fig. S1). Together, these findings indicate that both propofol and the photoaffinity derivative AziPm have the same selective disruption of kinesin processive movement likely reflecting a shared molecular mechanism.

#### Alkylphenol-based anesthetics bind specifically to the kinesin-1 and kinesin-2 motor domains in the presence of AMPPNP

Processive movement requires that one of the two motor heads of the kinesin dimer be strongly bound with the microtubule at any given time, otherwise the motor would fully detach from the microtubule when under load (38). The strongly bound states within the kinesin stepping cycle occur when the motor head, in complex with tubulin, is bound with ATP or without nucleotide altogether (Fig. 1). We hypothesized that propofol and AziPm would disrupt processive movement by interfering with one or both of the strongly bound states resulting in premature detachment from the microtubule. The nonhydrolysable ATP analogue, AMPPNP “locks” processive kinesins in a state similar to that thought for ATP-bound kinesin (39, 40). Therefore to examine potential mechanisms, we performed our studies with microtubule–kinesin complexes with or without AMPPNP to generate a system dominated by either the strongly bound nucleotide-free state or the ATP-bound state within the kinesin stepping cycle. To allow for semi-quantitative analysis of photolabeling of kinesin or tubulin and kinesin–tubulin complexes with or without AMPPNP we performed radiolabeling studies with tritiated AziPm ( $[^3\text{H}]\text{AziPm}$ ) (41, 42). We irradiated samples containing 10  $\mu$ M tubulin (microtubule) and 5  $\mu$ M kinesin with or without 1 mM AMPPNP in the presence of 10  $\mu$ M  $[^3\text{H}]\text{AziPm}$  with or without 400  $\mu$ M unlabeled propofol (to determine specificity). Following UV exposure, the proteins were precipitated with acetone, separated by SDS-PAGE, and visualized by Coomassie stain. Protein bands were excised and counted for radiolabel incorporation by scintillation counting (41) (Fig. S2). These values



## Identification of inhibitory propofol site within kinesins

**Table 1**

**[<sup>3</sup>H]AziPm photoaffinity radiolabeling of kinesin and microtubule–kinesin (MT–kinesin) complexes with and without AMPPNP and unlabeled propofol**

The MT–kinesin complex (10 μM MTs + 5 μM kinesin dimer) was preformed with or without (∅) 1 mM AMPPNP and with (+ propofol) or without (– propofol) 400 μM unlabeled propofol. Values are shown as mean ± S.E. of three experimental replicates.

Kinesin	MT–kinesin (∅)			MT–kinesin + AMPPNP	
		– Propofol	+ Propofol	– Propofol	+ Propofol
	<i>dpm</i> /(OD × mm <sup>2</sup> )	<i>dpm</i> /(OD × mm <sup>2</sup> )		<i>dpm</i> /(OD × mm <sup>2</sup> )	
K439	185.8 ± 39.25	304.3 ± 64.96	271.8 ± 50.78	702.8 ± 100.6	345.1 ± 61.33
KIF3AB	146.7 ± 25.18	165.9 ± 39.55	179.7 ± 32.0	458.2 ± 104.9	195.1 ± 44.82
KIF3AC	154.5 ± 37.39	197.7 ± 35.49	232 ± 43.76	559.6 ± 97.62	221.6 ± 38.94

**Table 2**

**[<sup>3</sup>H]AziPm photoaffinity radiolabeling of microtubules and microtubule–kinesin (MT–kinesin) complexes with and without AMPPNP and unlabeled propofol**

The MT–kinesin complex (10 μM MTs + 5 μM kinesin dimer) was preformed with or without (∅) 1 mM AMPPNP and with (+ propofol) or without (– propofol) 400 μM unlabeled propofol. Values are shown as mean ± S.E. of three experimental replicates.

Microtubule	MT–kinesin (∅)			MT–kinesin + AMPPNP	
		– Propofol	+ Propofol	– Propofol	+ Propofol
	<i>dpm</i> /(OD × mm <sup>2</sup> )	<i>dpm</i> /(OD × mm <sup>2</sup> )		<i>dpm</i> /(OD × mm <sup>2</sup> )	
Tubulin (K439)	106.4 ± 37.25	129.8 ± 49.51	152.6 ± 46.4	174.1 ± 73.09	216.2 ± 59.21
Tubulin (KIF3AB)	88.97 ± 24.0	154.6 ± 28.2	178.9 ± 12.9	297.4 ± 48.07	185.5 ± 50.5
Tubulin (KIF3AC)	65.1 ± 17.19	103.7 ± 29.95	151.1 ± 50.2	148.6 ± 22.66	137 ± 28.5

were normalized by the optical density of the Coomassie-stained protein band to prevent unwanted variation.

An increase in [<sup>3</sup>H]AziPm radiolabeling was observed for K439, KIF3AB, and KIF3AC in the presence of microtubules indicating the formation of binding sites associated with the microtubule–kinesin complexes rather than kinesin or microtubules alone. Radiolabeling was further increased with the introduction of 1 mM AMPPNP (Table 1). There was a 2–3-fold increase of the kinesin radiolabel photoincorporation in the microtubule–kinesin complexes in the presence of 1 mM AMPPNP compared with microtubule–kinesin complexes without the added nucleotide. To determine the specificity of [<sup>3</sup>H]AziPm binding, an excess of 400 μM propofol was included for each assay condition. Addition of 400 μM unlabeled propofol inhibited [<sup>3</sup>H]AziPm incorporation by 50–70% indicating that the site(s) present within the microtubule–kinesin–AMPPNP complexes show saturable binding and are shared between the [<sup>3</sup>H]AziPm photolabel and parent drug propofol. Considerable concentrations of parent drug are generally used to determine the specificity of binding sites due to the nonequilibrium nature of photoaffinity labeling (42, 43). Indeed over two times greater concentration of propofol was required to reduce labeling in the established protein target, the GABA type A (GABA<sub>A</sub>) receptor, to a similar degree as that used here for kinesin (44).

[<sup>3</sup>H]AziPm radiolabeling of microtubules across all conditions was less when compared with kinesins (Table 2). Only when microtubules were combined with KIF3AB and 1 mM AMPPNP was there a similar increase in tubulin photoincorporation (~1.9 fold; Table 2) as compared with radiolabel incorporation into kinesin. Furthermore, the addition of excess unlabeled propofol produced a trend toward inhibition of tubulin radiolabeling in the microtubule–KIF3AB complexes, suggesting a saturable site (Table 2). Interestingly minor increases in radiolabeling of tubulin were observed with addition of 400 μM propofol in KIF3AC and K439-containing systems indicative of either lower affinity and/or nonspecific binding. As a

whole, the increases in [<sup>3</sup>H]AziPm photolabeling of kinesin and the propofol inhibition of the photoincorporation suggest a specific and/or high affinity kinesin-binding site for propofol. This site appears to be dependent on the formation of the AMPPNP-promoted microtubule–kinesin complex where kinesin is strongly bound to the microtubule.

### Alkylphenol-based anesthetic-binding sites within the K439, KIF3B, and KIF3C catalytic motor head domains

We next identified the AziPm photolabeled residues within kinesin and/or tubulin of the microtubule–kinesin complexes with or without AMPPNP by mass spectrometry (MS) microsequencing. All kinesins, with or without AMPPNP, showed ample sequence coverage (80–96%) with K439 displaying 95 and 96% coverage in conditions with and without AMPPNP, respectively (Fig. S3–S6). Major isoforms of α (TBA4A)- and β (TBB4B)-tubulin showed >75% coverage across all experiments (Figs. S7 and S8). An increased number of AziPm adducts were identified in K439 in the microtubule–K439–AMPPNP complexes compared with the complexes with no added nucleotide (Fig. 3; Fig. S9). This trend was also observed for the KIF3B and KIF3C motors when the microtubule KIF3AC and KIF3AB complexes were photolabeled with or without AMPPNP (Fig. 3; Fig. S10–S12). All residues photolabeled by AziPm in KIF439, KIF3B, and KIF3C were located in the motor domain (Fig. 3). Interestingly, no AziPm adducts were detected within KIF3A peptides across all experiments. These observations suggest that the lack of inhibition by propofol and AziPm for homodimeric KIF3AA in single molecule motility studies was a result of KIF3A not binding propofol or AziPm. Moreover, the results indicate that KIFA in KIF3AB and KIF3AC was also unable to bind propofol or AziPm.

### AMPPNP-dependent formation of propofol-binding sites common between kinesin motor domains

To explore the results of our photolabeling experiments for each microtubule–kinesin complex, we aligned the kinesin

## Identification of inhibitory propofol site within kinesins

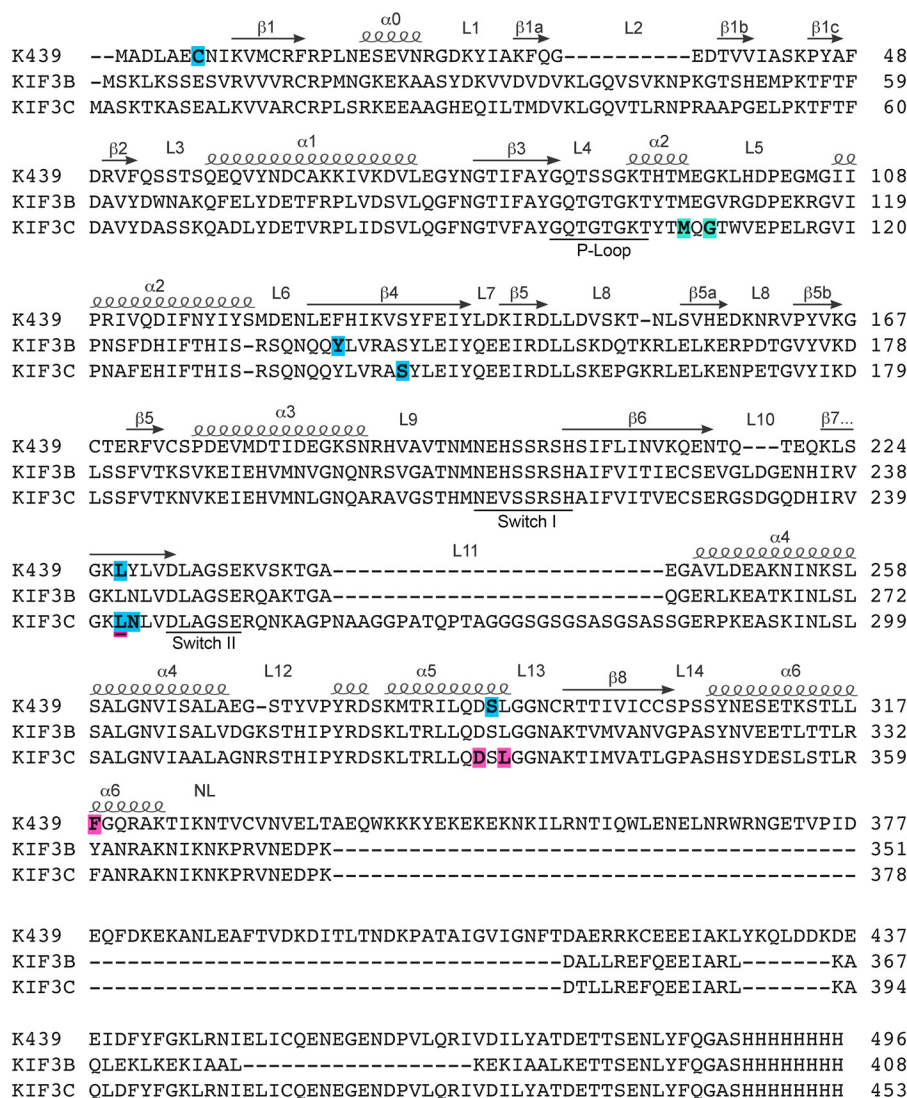


**Figure 3. Photolabeled residues in kinesin-1 and kinesin-2 motor domains.** Shown is alignment of kinesin motor domain sequences from kinesin-1 (K439) and kinesin-2 (KIF3B and KIF3C), with structural elements from kinesin-1 (KIF5B, PDB code 4HNA) provided above the alignment (30). Residues highlighted in *magenta* were photolabeled by AziPm in the no-nucleotide state for K439 (Phe<sup>318</sup>) and KIF3C (Leu<sup>242</sup>, Asp<sup>330</sup>, Leu<sup>332</sup>). Residues in the ATP-like AMPPPNP-bound state within the common allosteric binding site are highlighted in *cyan* for K439 (C7, Leu<sup>227</sup>, Ser<sup>289</sup>), KIF3B (Tyr<sup>138</sup>), and KIF3C (Ser<sup>144</sup>, Leu<sup>242</sup>, Asn<sup>243</sup>). The KIF3C residue Leu<sup>242</sup> was photolabeled by AziPm in the absence of nucleotide and in the presence of 1 mM AMPPNP, the ATP-like state (*cyan with magenta underline*). Additionally, residues photolabeled at a site unique to KIF3C in the presence of AMPPNP (Met<sup>107</sup>, Gly<sup>109</sup>) are highlighted in *teal*.

sequences with the X-ray crystal structures of the kinesin motor domain without nucleotide (PDB ID 4LNU) (29) or with adenosine diphosphate-aluminum fluoride (ADP-AlF<sub>4</sub><sup>-</sup>) (PDB ID 4HNA) (30) in complex with tubulin (Fig. S13). To further clarify propofol and AziPm-binding cavities, we substituted residues within kinesin motor head X-ray crystal structures to match the K439 sequence and analyzed both structures with Computed Atlas of Surface Topography of proteins (CASTp) web software (45). CASTp predicts binding cavities within proteins and provides the measurements as well as the contributing amino acid residues for the detected binding pockets. Pockets of sufficient volume to accommodate at least one propofol or AziPm molecule (>200 Å<sup>3</sup>) (Fig. S14) were investigated with docking experiments using AutoDock Vina (46) to further refine potential binding sites. The docking regions were set to include all amino acid residues that were predicted to contribute at least one atom of the side chain or backbone to the bind-

ing pocket lining. Additionally, all residue side chains were made flexible within the docking experiment to provide an estimate of ligand binding energies. Within each structure, atoms from the majority of photolabeled residues detected by MS in the microtubule–kinesin complexes with or without AMPPNP were found to line computationally defined binding pockets with appropriate volumes.

Docking within the kinesin motor domain of the tubulin–kinesin complex without nucleotide indicated that an interior pocket between the  $\alpha^4$  and  $\alpha^6$  helices and  $\beta$ -strands  $\beta^3$ ,  $\beta^7$ , and  $\beta^8$  would accommodate propofol and AziPm with poses represented within the site (Fig. 4A). A continuous solvent accessible pocket was also indicated between the  $\alpha^4$  and  $\alpha^5$  helices and  $\beta$ -strands  $\beta^1$  and  $\beta^3$  for both ligands (Fig. 4A). Photolabeled residues identified within microtubule–kinesin complexes without nucleotide are in close proximity to the highest scored poses. Specifically photolabeled residues located at  $\alpha^5$  and  $\alpha^6$

## Identification of inhibitory propofol site within kinesins

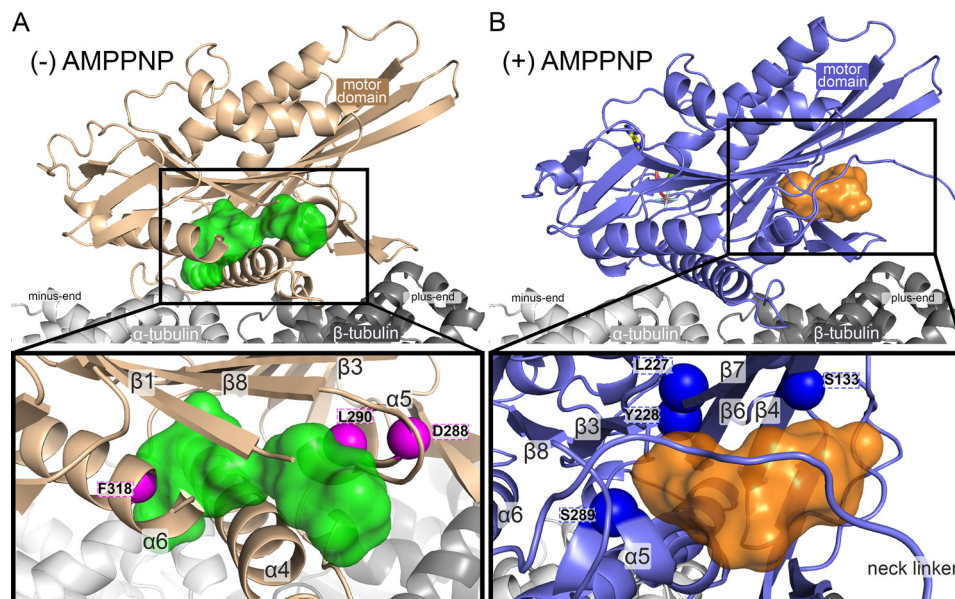


**Figure 4. Location of predicted propofol and AziPm-binding pockets and associated photolabeled residues in microtubule-kinesin complexes without and with AMPPNP.** *A*, side and focused view of the X-ray crystal structure of kinesin motor head in complex with tubulin in the absence of nucleotide (PDB ID 4LNU) (29) representing photolabeled microtubule-kinesin complexes without (–) AMPPNP. The green Connolly surface representations highlight the highest scored poses for five propofol and five AziPm as predicted by AutoDock Vina (46) within the CASTp (45) predicted binding cavity (see appendix Fig. S11). Magenta spheres indicate the  $\alpha$ -carbon atoms of Phe<sup>318</sup> photolabeled in K439 and Asp<sup>288</sup> and Leu<sup>290</sup> that correspond with the photolabeled residues Asp<sup>330</sup> and Leu<sup>332</sup> in KIF3C, respectively. *B*, side and focused view of the X-ray crystal structure of ADP-AIF<sub>4</sub><sup>–</sup>-bound kinesin motor head in complex with tubulin (PDB ID 4HNA) (30) representing photolabeled microtubule-kinesin complexes with (+) AMPPNP. The orange Connolly surface representations highlight five propofol and five AziPm in the highest scored poses predicted by AutoDock Vina (46) within the CASTp (45) predicted binding cavity (see Fig. S14). Blue spheres indicate the  $\alpha$ -carbon atoms of the photolabeled residue in K439 (Ser<sup>289</sup>), photolabeled residues in KIF3C (Ser<sup>144</sup> and Asn<sup>243</sup>), corresponding with Ser<sup>133</sup> and Tyr<sup>226</sup> in K439, respectively, and the photolabeled residue in both K439 (Leu<sup>227</sup>) and KIF3C (corresponding with Leu<sup>242</sup>). ADP-AIF<sub>4</sub><sup>–</sup> is shown in stick representation and a Mg<sup>2+</sup> ion is shown as a light green sphere. All residues within predicted binding sites were made flexible in AutoDock Vina, whereas the backbone structure remained rigid during docking experiments.

align well with both the CASTp-predicted binding site and distances from highest scored poses generated by AutoDock Vina (Fig. 4A). Propofol is expected to be highly dynamic in its binding site, and thus more than one pose is likely to reflect reality, and is the basis for multiple photolabeled residues.

Significant conformational changes within the motor head are observed when comparing the no nucleotide and ADP-AIF<sub>4</sub><sup>–</sup>-bound kinesin X-ray crystal structures (29). These structural changes are generally described as rigid movements involving three distinct subdomains: P-loop and Switch I/II subdomains, and the microtubule-binding interface (29). Namely, when the microtubule-kinesin complex binds ATP, the nucleotide cleft closes resulting in concerted rotations of the P-loop and Switch I/II subdomains (29, 31). The movement of the subdomains results in the obstruction of the interior pocket that was predicted by CASTp in the no nucleotide-bound kinesin motor. Instead, within the ADP-AIF<sub>4</sub><sup>–</sup>-bound microtubule-kinesin complex, CASTp predicted a large cavity located mainly between the  $\alpha$ 5 helix,  $\beta$ -strands  $\beta$ 3,  $\beta$ 4,  $\beta$ 6, and  $\beta$ 7 and the neck linker (Fig. S14). Propofol and AziPm displayed similar poses in the cavity, with the highest scored poses by AutoDock Vina within the  $\alpha$ 5 helix and  $\beta$ -strands  $\beta$ 4,  $\beta$ 6, and  $\beta$ 7 (Fig. 4B). Again photolabeled residues by AziPm were consistently near poses generated by docking, specifically photolabeled residues located within  $\beta$ -strands  $\beta$ 4 and  $\beta$ 7 (Fig. 4B).

Together photoaffinity labeling experiments provide evidence that alkylphenol-based anesthetics bind within microtubule-kinesin complexes both in the presence and absence of AMPPNP. Indeed [<sup>3</sup>H]AziPm radiolabeling, which

provides a quantitative assessment of photolabeling, aligns with these findings. Although not significant, photoincorporation may be increased within microtubule-kinesin complexes without nucleotide compared with samples only containing dimeric kinesin. However, given that [<sup>3</sup>H]AziPm photoincorporation was comparatively lower and propofol did not inhibit the radiolabeling within complexes without nucleotide suggests that the pocket identified within AMPPNP-bound microtubule-kinesin complexes better represents a higher affinity and/or propofol-specific site. An additional compelling feature was the photolabeling of similar putative binding pockets identified within the AMPPNP-bound complex relative to no nucleotide-bound microtubule-kinesin complex, namely those photolabeled residues within  $\alpha$ 5 helix and  $\beta$ -strands  $\beta$ 1 and  $\beta$ 7 (Fig. S13). These results suggest that alkylphenol-based anesthetics may also bind to an intermediate state between the two static crystal structures represented. Additional studies and increased understanding of these intermediate conformations will be needed to test this potential mechanism.

### Additional kinesin-specific alkylphenol-based anesthetic binding sites

An additional site was photolabeled by AziPm in KIF3C (Met<sup>107</sup> and Gly<sup>109</sup>) located at an interface of the P-loop and Switch I/II domains that were near, but not contributing to, the nucleotide-binding site (Fig. 5). Furthermore, despite the comparative abundance and proximity to the kinesin motor, only one residue within  $\beta$ -tubulin was photolabeled by AziPm and only in the KIF3AB ATP-like system (Met<sup>257</sup>; Fig. 5). This res-



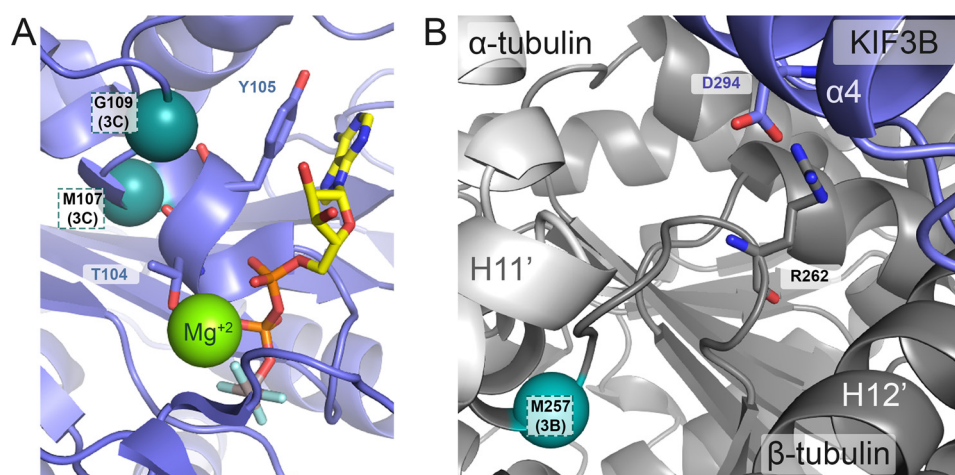


**Figure 5. AziPm photolabeled residue identified in secondary sites for KIF3C and KIF3AB  $\beta$ -tubulin within the AMPPNP-bound microtubule–kinesin complexes.** *A* and *B*, expanded views of the X-ray crystal structure of ADP-AIF<sub>4</sub><sup>−</sup>-bound kinesin motor head in complex with tubulin (PDB ID 4HNA) to represent the microtubule–kinesin complexes with AMPPNP. *A*, photolabeled residues (Met<sup>107</sup> and Gly<sup>109</sup>) within the KIF3C second the photolabeled pocket from the nucleotide-binding site are labeled accordingly. ADP-AIF<sub>4</sub><sup>−</sup> is shown in stick representation and a magnesium ion is shown as a *light green sphere*. *B*, photoaffinity labeled residue (Met<sup>257</sup>) in  $\beta$ -tubulin within KIF3AB microtubule–kinesin complexes with AMPPNP and the residue's relationship to TUBB3 Arg<sup>262</sup>. The  $\alpha$ -carbon of photolabeled residues are represented as *teal spheres* and are labeled accordingly.

idue is close to the human TUBB3 R262H and R262A mutation sites that impair the motility and ATPase activity of the kinesin motor (47–50). It is not clear how these secondary sites contribute to AziPm and propofol's mechanism(s), however, they may hint toward additional kinesin-specific effects. Ultimately, the conserved site shared by K439, KIF3B, and KIF3C at the junction of Switch I/II subdomain and microtubule-binding interface is likely to be the main contributor to the common effects of alkylphenol-based anesthetics to decrease kinesin run length, whereas preserving velocity.

## Discussion

This study indicates that propofol binds at a site allosteric to the catalytic site within the kinesin motor head, which forms in the ATP-bound state, leading to premature detachment of anterograde processive kinesins and their cargos from the microtubule (Fig. 1). To our knowledge, this common site identified in K439, KIF3B, and KIF3C is the first evidence of a drug-gable inhibitory site within the interface of the Switch I/II subdomain and the microtubule–kinesin interface. Given that the mechanism of kinesin processivity appears to rely on the collective movement of these subdomains, the binding of inhibitors at their interfaces would be a rational mechanism to alter the kinesin motor head internal reorganization and impair motor head coordination for the kinesin stepping cycle. Indeed, interfacial binding between motor head subdomains has been previously observed for other kinesin allosteric inhibitors (51–53). However, these sites are located at alternative sites within kinesin compared with the common binding site identified for propofol and these inhibitors affect both the velocity and ATPase activity. We hypothesize that propofol binding at the Switch I/II subdomain and microtubule interface would promote the premature formation of a weak binding state that disrupts motor head coordination resulting in motor detachment. Such a mechanism, largely distinct from ATP hydrolysis, would be predicted to result in the decreased kinesin run length, whereas maintaining normal velocity. Furthermore, if

propofol binding occurred when only one motor head was in complex with the microtubule during the kinesin mechanochemical cycle, then there would be an increased likelihood of premature detachment (*E2* and *E3*, Fig. 1). More investigations into the structure and/or kinetics of propofol binding within specific kinesins and their intermediate states will help to resolve these subtle mechanistic distinctions.

The nanomolar potency to inhibit kinesin processivity is in contrast to other functionally influenced protein targets identified for propofol. Indeed affinities for many binding targets and the plasma concentrations often associated with propofol are within the low micromolar range. Many general anesthetics are considered hydrophobic drugs, with propofol water/octanol partition coefficient of  $\sim 3.79$ . As a consequence it is likely that propofol concentrates in more hydrophobic biological microdomains such as lipid bilayers. We anticipate that the conditions of the Qdot single molecule assay would be reflective of the cytosol and therefore the significant inhibition of kinesin processivity at nanomolar concentrations would, within a biological context, be clinically relevant. Further studies to determine the impact on cellular, or more likely, the neuronal circuit are required to evaluate the contribution of this effect on propofol's mechanism of action.

Previously we showed that the general anesthetic propofol significantly reduced the run-length potential of processive kinesins without altering their velocity of movement (26). Additionally, this study demonstrated that the decrease was specific to the propofol 1-hydroxyl, because a fluorine-substituted derivative lacking anesthetic activity also had no effect on kinesin processivity. The current study confirms that the photolabel analogue AziPm has a similar unique functional activity to propofol, and connects this activity to a specific allosteric binding site within kinesin. The hypnotic effects of general anesthetics like propofol are typically attributed to ligand-gated ion channels, such as the GABA<sub>A</sub> receptor (54). However, studies on mice lacking various subunits of the GABA<sub>A</sub> receptor still

## Identification of inhibitory propofol site within kinesins

exhibit a hypnotic response to anesthetic exposure. Furthermore, the data that have been reported for various other molecular targets are insufficient to establish these ion channels as both necessary or sufficient to produce all the various components that constitute the state of anesthesia, as well as the many adverse effects (55).

Propofol's potent ability to cause a 40–60% reduction in kinesin run length (26) provides an additional molecular mechanism for altering neuronal function: a disruption of intracellular transport. Indeed various mechanisms that require kinesin, including neurite growth and specification as well as vesicle exocytosis, are influenced by anesthetics (56, 57). Nevertheless, an important physiological role for this propofol–kinesin interaction remains to be demonstrated. In summary, this work provides important structural clues of a novel molecular mechanism for disrupting kinesin processivity and broadens the prospective targets involved in propofol pharmacology.

### Experimental procedures

#### Kinesin-1 K439 cloning and expression

The expression construct for human kinesin-1 K439 was a custom gene synthesis from GenScript (Piscataway, NJ) as an insert in the pET24d expression vector between NcoI and BamHI restriction sites. This construct encoded the first 439 residues of *Homo sapiens* KIF5B, a C terminally fused EB1 sequence that matched the coiled-coil registry of the helix to create stable dimers (bold), a TEV protease site (italicized) with linker residues (plain font), and a His<sub>8</sub> tag (underlined): K439, *Hs* KIF5B (Met<sup>1</sup>–Ile<sup>439</sup>)-**DFYFGKLRNIELICQENEGENDPVLQRIVDILYATDETTSE**; *NLYFQGASHHHHHHHH* (predicted  $M_r = 56,538$ ).

K439 was bacterially expressed based on the protocol for kinesin-1 K560 as previously reported (26). Briefly, *Escherichia coli* BL21-CodonPlus (DE3)-RIL cells (Stratagene, La Jolla, CA) were transformed with the K439 plasmid followed by selection on lysogeny broth (LB) plates containing 50 μg/ml of kanamycin and 10 μg/ml of chloramphenicol. Positive colonies were selected and grown in LB liquid culture containing the same selective antibiotics at 37 °C until they reached  $A_{600}$  of 0.4–0.5. Cultures were then chilled on an ice bath to 16 °C before expression was induced by the dropwise addition of 0.1 mM isopropyl β-D-1-thiogalactopyranoside (IPTG), which continued for ~16–18 h at 16 °C shaking at 185 rpm.

#### Kinesin-2 KIF3 cloning and expression

Preparation of mouse KIF3AB constructs was described in detail previously (58). Briefly, each expression plasmid encoded the native N-terminal motor domain sequence through the native helix α7 followed by a C terminally fused synthetic heterodimerization helix (SHD; bold) motif containing either an acidic (AHD) or basic (BHD) sequence that generated pairwise stabilized heterodimeric motors. The SHD was followed by a TEV protease site (italicized) with linker residues (plain font) and affinity purification tags (underlined). The use of a StrepII tag on KIF3A-AHD combined with the use of a His<sub>8</sub> tag on KIF3B-BHD provided the ability to purify stable heterodimers with sequential affinity purification steps: KIF3A(Met<sup>1</sup>–Glu<sup>376</sup>)-**LEKEIAALEKEIAALEKTTSENLYFQGASNWSHP-**

**QFEK** (predicted  $M_r = 46,341$ ); KIF3B(Met<sup>1</sup>–Lys<sup>371</sup>) **LKEKI-AALKEKIAALKETTSENLYFQGASHHHHHHHH** (predicted  $M_r = 45,790$ ).

Preparation of mouse KIF3AC was described in detail previously (59), but briefly the design replicated the strategy used for KIF3AB with the exception that the native N-terminal motor through α7 was followed by a C terminally fused sequence of EB1 for dimerization (bold) that matched the coiled-coil registry of the native helix, a TEV protease site (italicized) with linker residues (plain font) and affinity purification tags (underlined). As with KIF3AB, the use of the StrepII tag on KIF3A combined with a His<sub>8</sub> tag on KIF3C allowed for sequential purification steps to generate pure, stable heterodimeric KIF3AC: KIF3A-EB1, KIF3A(Met<sup>1</sup>–Leu<sup>374</sup>)-**DFYFGKLRNIELICQENEGENDPVLQRIVDILYATDETTSENLYFQGASNWSHP-QFEK** (predicted  $M_r = 48,559$ ); KIF3C, KIF3C(Met<sup>1</sup>–Leu<sup>396</sup>)-**DFYFGKLRNIELICQENEGENDPVLQRIVDILYATDETTSENLYFQGASHHHHHHHH** (predicted  $M_r = 49,759$ ).

This same KIF3C construct was used for generating homodimeric KIF3CC for the experiments reported herein. The constructs used to express KIF3AA and KIF3BB differ from those detailed above for heterodimeric motors. Rather than use SHD for heterodimerization, KIF3A and KIF3B homodimeric clones utilized the EB1 dimerization strategy (bold) described above for KIF3C, a TEV protease site (italicized) with linker residues (plain font), and a His<sub>8</sub> tag for purification (underlined): KIF3A (Met<sup>1</sup>–Leu<sup>374</sup>)-**DFYFGKLRNIELICQENEGENDPVLQRIVDILYATDETTSENLYFQGASHHHHHHHH** (predicted  $M_r = 48,502$ ); KIF3B(Met<sup>1</sup>–Leu<sup>369</sup>)-**DFYFGKLRNIELICQENEGENDPVLQRIVDILYATDETTSENLYFQGASHHHHHHHH** (predicted  $M_r = 48,011$ ).

All KIF3 motors were bacterially expressed as previously reported (26, 58) in *E. coli* BL21-CodonPlus (DE3)-RIL cells (Stratagene). Heterodimeric KIF3AB and KIF3AC resulted from bacteria that were co-transformed by electroporation with the two appropriate motor expression plasmids, followed by selection on lysogeny broth (LB) plates containing 100 μg/ml of ampicillin, 50 μg/ml of kanamycin, and 10 μg/ml of chloramphenicol. Homodimeric KIF3AA, KIF3BB, and KIF3CC each resulted from bacterial transformation with a single homodimer-designed plasmid followed by selection on LB plates containing 100 μg/ml of ampicillin and 10 μg/ml of chloramphenicol. Positive colonies were selected and grown in LB liquid culture containing the same selective antibiotics at 37 °C until they reached  $A_{600}$  of 0.4–0.5. Cultures were then chilled on an ice bath to 16 °C before expression was induced by the dropwise addition of 0.1 mM IPTG, which continued for ~16–18 h at 16 °C shaking at 185 rpm.

#### Purification of kinesin dimers

For all kinesins reported herein, cultures were subjected to centrifugation to collect cell pellets, which were then resuspended by spinning at 4 °C with the addition of lysis buffer to 10 ml/g of cells. Lysis buffer contained 10 mM sodium phosphate buffer, pH 7.2, 300 mM NaCl, 2 mM MgCl<sub>2</sub>, 0.1 mM EGTA, 0.02 mM ATP, 1 mM DTT, 10 mM phenylmethylsulfonyl fluoride, and 30 mM imidazole. Cells were lysed by the addition of 0.2 mg/ml of lysozyme to the resuspended cells with continued



stirring for 50 min at 4 °C, followed by three replicate cycles of freezing in liquid N<sub>2</sub> and thawing in a 37 °C water bath. Lysate was then clarified by ultracentrifugation and applied to a His-Trap FF Ni<sup>2+</sup>-NTA column (GE Healthcare) that had been pre-equilibrated with Ni<sup>2+</sup>-NTA binding buffer (20 mM sodium phosphate buffer, pH 7.2, 300 mM NaCl, 2 mM MgCl<sub>2</sub>, 0.1 mM EGTA, 1 mM DTT, 0.02 mM ATP, and 30 mM imidazole).

For K439, the loaded column was then washed with K439 Wash Buffer (20 mM sodium phosphate buffer, pH 7.2, 300 mM NaCl, 2 mM MgCl<sub>2</sub>, 0.1 mM EGTA, 1 mM DTT, 0.02 mM ATP, and 50 mM imidazole) until baseline absorbance was established. His-tagged K439 was then eluted with a linear gradient (Ni<sup>2+</sup>-NTA wash buffer: 50–400 mM imidazole, pH 7.2). Positive elution fractions were pooled, concentrated, and initially dialyzed overnight at 4 °C against K439 Dialysis Buffer (20 mM HEPES, pH 7.2, with KOH, 0.1 mM EDTA, 0.1 mM EGTA, 5 mM magnesium acetate, 50 mM potassium acetate, 1 mM DTT plus 300 mM NaCl). Three additional dialysis steps were conducted the following day for 60 min, each at 4 °C to gradually decrease the concentration of NaCl (K439 Dialysis Buffer: 200 mM, 150 and 100 mM NaCl). The final dialysis buffer for K439 at 100 mM NaCl also included 5% sucrose.

The purification of kinesin-2 motors (KIF3AC, KIF3AB, KIF3AA, KIF3BB, and KIF3CC) has been reported previously (26, 58), but briefly the loaded HisTrap Ni<sup>2+</sup>-NTA column was then washed with excess Ni<sup>2+</sup>-NTA binding buffer, and motors were eluted with a linear gradient (Ni<sup>2+</sup>-NTA binding buffer: 30–300 mM imidazole, pH 7.2). For homodimeric motors, positive elution fractions were pooled, concentrated, and dialyzed at 4 °C overnight in 20 mM HEPES, pH 7.2, with KOH, 0.1 mM EDTA, 0.1 mM EGTA, 5 mM magnesium acetate, 50 mM potassium acetate, 1 mM DTT plus 100 mM NaCl, and 5% sucrose. For heterodimeric motors, positive HisTrap Ni<sup>2+</sup>-NTA fractions were pooled and transferred to a StrepII Tactin<sup>TM</sup> column (StrepTrapII HP, GE Healthcare) that had been pre-equilibrated with StrepII column buffer (20 mM sodium phosphate buffer, pH 7.2, 300 mM NaCl, 2 mM MgCl<sub>2</sub>, 0.1 mM EGTA, 1 mM DTT, 0.2 mM ATP). The loaded StrepII column was washed with excess StrepII column buffer to return to baseline absorbance, followed by elution in StrepII column buffer plus 2.5 mM desthiobiotin. Fractions from the StrepII column were analyzed by SDS-PAGE to identify only fractions containing a 1:1 ratio of each KIF3 polypeptide. These fractions were then pooled, concentrated, and dialyzed at 4 °C overnight in 20 mM HEPES, pH 7.2, with KOH, 0.1 mM EDTA, 5 mM magnesium acetate, 50 mM potassium acetate, 1 mM DTT, 5% sucrose, 100 mM NaCl. The purity of all motors was confirmed by both analytical gel filtration on an HPLC gel filtration column (Superose<sup>TM</sup> 10/300, GE Healthcare Life Sciences) and SDS-PAGE. Note that the purification tags were not cleaved for the experiments reported herein. Typical yields for purified motors from bacterial expression were 1.7–3 mg/g of *E. coli*. Predicted molecular weights based on amino acid residue sequence are as follows: K439 at 113,076; KIF3AC at 98,317; KIF3AB at 92,131; KIF3AA at 97,000; KIF3BB at 96,022; and KIF3CC at 99,518. Prior to each experiment, kinesin aliquots were thawed, clarified for 10 min at 4 °C (Beckman Coulter TLX Optima Ultracentrifuge, TLA-100 rotor, 313,000 × g), and the protein concentration was

determined using the Bio-Rad protein assay with IgG as a protein standard.

### Single molecule motility assays

Kinesin motors were visualized by attachment of streptavidin-coated quantum dots (Qdot 525-Streptavidin conjugate, Life Technologies) to the His-tagged C terminus. Qdots were preincubated with biotinylated-Penta-His antibody (Qiagen) at a 1:1 ratio (200 nM each) for 60 min at room temperature in PME80 buffer (80 mM PIPES, pH 6.9, with KOH, 5 mM MgCl<sub>2</sub>, and 1 mM EGTA). To this mixture, His-tagged kinesin dimers were added to a final concentration of 20 nM dimer and incubated for an additional 60 min at 4 °C. This process generated a working stock of Qdot-labeled motors at a ratio of 1:10 kinesin dimer:Qdots (20 nM dimer, 200 nM Qdot-antibody complex). According to a Poisson distribution, 9% of the Qdots in this working stock are estimated to have one motor bound and 0.5% with ≥2 motors bound. Previous KIF3 experiments confirmed that a 1:10 ratio of kinesin motors to Qdots was sufficient for single molecule conditions (59).

Long microtubule tracks (13–30 μm) used for microscopy were polymerized as previously described (59) from lyophilized X-rhodamine tubulin (Cytoskeleton, Inc., Denver, CO). Tubulin was resuspended in PME80 buffer containing 10% glycerol, followed by incubation on ice for 5 min in the presence of 1 mM MgGTP. The tubulin was then centrifuged at 16,000 × g for 10 min at 4 °C (Galaxy 16D Micro 1816 centrifuge, VWR, Bridgeport, NJ). The clarified supernatant that contained soluble tubulin was transferred to a new tube, and polymerization was conducted at 37 °C for 20 min. The polymerized microtubules were then stabilized by the addition of paclitaxel (final 33 μM final concentration) and incubated for an additional 10 min. This procedure yields a final microtubule stock at 30 μM tubulin polymer.

Perfusion chambers were formed by mounting a silanized coverslip on a glass slide with strips of double-sided tape to generate a 10-μl flow cell. Chambers were first incubated with 0.4% rat anti-α-tubulin antibody (ABD Serotec, Raleigh, NC) for 5 min followed by surface blocking with 5% Pluronic F-127 (Sigma) for 5 min.

X-rhodamine microtubules (30 μM stock) were diluted 1:300 in PME80 supplemented with paclitaxel to 22 μM to generate a final microtubule concentration at 0.1 μM. Microtubules were then introduced into the perfusion chamber and incubated for 10 min. Unbound microtubules were removed by washing the chamber with excess PME80 supplemented with 10 mM DTT and 20 μM paclitaxel. For kinesin-2 motors, the working stock of Qdot-motor complexes (20 nM dimer/200 nM Qdot-antibody complex) was then added to an Activity Buffer (PME80, 0.5% Pluronic F-127, 30 μM paclitaxel, 125 μg/ml of BSA, 50 μM DTT, 25 mM glucose, 0.2 mg/ml of glucose oxidase, 175 μg/ml of catalase, 0.3 mg/ml of creatine phosphokinase, 2 mM phosphocreatine, 1 mM MgATP, 5% DMSO ± 10 μM AziPm or Propofol) to dilute the motors 10 times and give a final concentration of 2 nM Qdot-motor complex in the chamber. Adding Activity Buffer to the perfusion chamber activated motor activity, and chambers were imaged immediately.

## Identification of inhibitory propofol site within kinesins

For Qdot–K439 complexes, 0.5 mM AMPPNP was required to generate the microtubule–K439–Qdot complex. Therefore, the setup of the perfusion chamber was altered such that immediately following the 10-min microtubule binding step, Qdot–K439 complexes were introduced in PME80 supplemented with 10 mM DTT, 20  $\mu$ M paclitaxel, and 0.5 mM Mg-AMPPNP and incubated in the chamber for 5 min. This step replaced the wash step to remove unbound microtubules. Qdot–K439 complexes were then activated by introduction of Activity Buffer containing 1 mM MgATP.

### TIRF microscopy and image acquisition

Single molecule motility chambers were imaged by TIRF microscopy at 25 °C using a Zeiss Inverted Axio Observer Z1 MOT fluorescence microscope with the  $\times 100$  oil 1.46 N.A. Plan-Apochromat objective (Carl Zeiss Microscopy, Inc., Jena, Germany) and an incubation hood as previously described (59). Digital images were collected with a Hamamatsu electron multiplier EM-CCD digital camera using the AxioVision 4.8.2 software package. The images generated were 512  $\times$  512 pixels with 0.16  $\mu$ m/pixel in both *x*- and *y*-planes. Qdot–kinesin complexes were tracked by imaging at 488 nm (5% laser power, 100 ms exposure) every  $\sim 0.5$  s for 5 min. Reference images of the X-rhodamine microtubule tracks were taken at 564 nm (2% laser power, 300 ms exposure) both before and after acquisition of data in the Qdot channel. Qdot videos were then overlaid with the microtubule image using NIH ImageJ software.

### Data analysis

Single molecule motility was analyzed with ImageJ and the MultipleKymograph plugin (J. Rietdorf and A. Seitz, European Molecular Biology Laboratory, Heidelberg, Germany). Mean velocity  $\pm$  S.E. was determined from histograms of velocity data with an applied Gaussian function. Mean run lengths were determined from histograms of run length data with an applied single exponential decay fit according to the following equation,

$$y = y_0 + A^{(-x/l)} \quad (\text{Eq. 1})$$

where *A* is the maximum amplitude and *l* is the mean run length reported  $\pm$  S.E. The first bin of run-length histograms was masked from the fit due to the resolution limit of the TIRF microscope ( $<0.25$   $\mu$ m).

To ensure that the maximum run-length potential was examined, Qdot–kinesin complexes were excluded from analysis if they reached the end of the microtubule before falling off, paused at the microtubule end, or began or ended a run outside the timescale of the experiment. Only long microtubule tracks were used for data analysis, which allowed for collection of both long and short runs on the same tracks, thereby avoiding data bias. Statistical analysis to compare mean values from single molecule datasets was conducted with a Student's *t* test using an  $\alpha$ -reliability level of 5%.

### Preparation of microtubules for photoaffinity labeling

Aliquots of purified bovine brain tubulin were diluted with an equal volume of PM buffer (100 mM PIPES, pH 6.9, 5 mM

magnesium acetate, 1 mM EGTA) and cold-depolymerized on ice for 30 min in the presence of 1 mM GTP. Tubulin was then clarified by centrifugation at 16,000  $\times g$  for 15 min at 4 °C and the soluble tubulin supernatant was removed to a fresh tube. Soluble tubulin was then polymerized by incubation at 37 °C, and microtubules were stabilized by the addition of 20  $\mu$ M Taxol. Microtubules were pelleted at 16,000  $\times g$  at ambient temperature and resuspended in ATPase buffer (20 mM HEPES, pH 7.2, 5 mM magnesium acetate, 0.1 mM EDTA, 0.1 mM EGTA, 50 mM potassium acetate, 5% sucrose) containing 1 mM DTT and 40  $\mu$ M Taxol. The concentration of tubulin polymer was determined by Lowry assay with BSA as a protein standard.

### Photoaffinity radiolabeling

Reaction samples contained final concentrations of 10  $\mu$ M tubulin, 5  $\mu$ M kinesin dimer, with or without 1 mM Mg-AMPPNP in ATPase buffer containing 1 mM DTT, 40  $\mu$ M paclitaxel, 10  $\mu$ M [ $^3\text{H}$ ]meta-azipropofol ([ $^3\text{H}$ ]AziPm), and 6% methanol with or without 400  $\mu$ M propofol. Reactions were prepared in the following order: 1) ATPase buffer containing DTT and paclitaxel, 2) tubulin dimer, 3) kinesin, 4) AMPPNP or buffer, then 5) [ $^3\text{H}$ ]AziPm in methanol with or without propofol. Immediately after preparation, half of the reaction mixture was placed in a 1-mm path length quartz cuvette and exposed to UV irradiation at 350 nm, RPR-3000 Rayonet lamp through a WG295 295-nm low-pass glass filter (Newport Corporation) for 25 min. The remaining half of the reaction mixture was used as a matched non-UV irradiated control. After UV exposure samples were added to 4 volumes chilled acetone and proteins were precipitated overnight at  $-20$  °C. Protein was pelleted for 20 min at 16,000  $\times g$  at 4 °C then gently washed twice with 300  $\mu$ l of chilled acetone. Protein pellets were air-dried before resuspension in 50  $\mu$ l of 50 mM Tris-HCl, pH 8.0, 1% Triton X-100, and 0.5% SDS. Insoluble debris was pelleted by centrifugation at 16,000  $\times g$ . The supernatant was removed, and protein content was determined by BCA assay. SDS-PAGE sample buffer at  $\times 5$  was added, and samples were heated for 3 min at 90 °C. Total sample protein (1–3  $\mu$ g) was separated on a 10% SDS-PAGE gel. Gels were stained and fixed in 10% acetic acid, 50% methanol, 0.5% Coomassie Blue G-250 in ddH<sub>2</sub>O and destained with 10% acetic acid + 10% methanol in ddH<sub>2</sub>O. After destaining the gels were washed three times with ddH<sub>2</sub>O. Gels were scanned on a Bio-Rad GS-800 calibrated densitometer with quantification using the accompanying Quantity One software. To correct for the differences in optical density measurements caused by the background staining of an individual gel, the background was subtracted with a box drawn in a blank gel lane adjacent to the sample band and the mean optical density (O.D.) multiplied by the band area was recorded from contoured bands (OD  $\times$  mm<sup>2</sup>). Representative gel images of protein bands are shown in Fig. S2.

Bands were excised and placed into scintillation vials. One ml of 30% hydrogen peroxide (v/v %) was added, and vials were incubated overnight at 65 °C to dissolve the polyacrylamide. Samples were then cooled to ambient temperature before the addition of 10 ml of EcoLite(+) liquid scintillation mixture. Samples were mixed vigorously and incubated at ambient temperature overnight before counting with a PerkinElmer Life

Sciences Tri-Carb 2800TR instrument. The measured disintegrations per minute (dpm) for each excised band was normalized to the optical density ( $OD \times mm^2$ ) of the protein band to correct for the amount of protein applied for scintillation counting and control for unwanted variation. Dpm values not normalized to the optical density are shown in [Tables S1 and Table S2](#). Radioactivity within the SDS-PAGE gel not caused by the photoaffinity radiolabeling experiment was corrected by substrating a background control of an excised 75-kDa protein ladder band for each gel as well as the associated non-UV-irradiated protein bands for kinesin or tubulin samples. Non-UV-irradiated protein samples displayed <5% of the measured radioactivity relative to UV-irradiated samples. Radiolabeling experiments were conducted in three technical replicates to insure the reliability of single values and are represented as the mean  $\pm$  S.E.

### Photoaffinity labeling for microsequencing

Reaction samples were prepared similar to those mentioned above. Briefly, samples were prepared with final concentrations of 10  $\mu$ M tubulin, 5  $\mu$ M kinesin dimer in ATPase buffer containing 1 mM DTT, 40  $\mu$ M paclitaxel, 10  $\mu$ M AziPm, and <0.01% DMSO vehicle with or without 1 mM Mg-AMPPNP. Samples were then exposed to UV irradiation, and 20  $\mu$ g of protein was precipitated using 4 volumes of chilled acetone, and proteins were precipitated overnight at  $-20^\circ\text{C}$ . Protein was pelleted for 20 min at  $16,000 \times g$  at  $4^\circ\text{C}$  and then gently washed twice with 300  $\mu$ l of chilled acetone. Protein pellets were resuspended in 20  $\mu$ l of 0.2% ProteaseMax<sup>TM</sup> Surfactant Enhancer (Promega; w/v%) in 50 mM  $\text{NH}_4\text{HCO}_3$ . Samples were then diluted with 74  $\mu$ l of 50 mM  $\text{NH}_4\text{HCO}_3$  prior to the addition of 1  $\mu$ l of 0.5 M DTT and incubation at  $56^\circ\text{C}$  for 20 min. Protein was then alkylated with the addition of 2.7  $\mu$ l of 0.55 M iodoacetamide and incubation in the dark at room temperature for 20 min. Subsequently, 1  $\mu$ l of 0.1 M  $\text{CaCl}_2$  and 1  $\mu$ l of 1% ProteaseMax<sup>TM</sup> Surfactant Enhancer (w/v%) was added, and proteins were digested overnight at  $37^\circ\text{C}$  using sequencing grade trypsin (Promega) at  $\sim$ 1:20 protease:protein (w/w) ratio. To stop digestion, TFA was added to 0.5% (v/v%) and samples were incubated at room temperature for 10 min. Samples were snap frozen with dry ice and stored at  $-80^\circ\text{C}$  until further processing. Insoluble debris was removed by centrifugation at  $16,000 \times g$  and the soluble peptide digest was desalted using C18 stage tips prepared in-house. The final elution was dried by SpeedVac and prior to MS analysis was resuspended in 0.1% formic acid (v/v %).

### Mass spectrometry

Desalted peptides were analyzed on an Orbitrap Elite<sup>TM</sup> Hybrid Ion Trap-Orbitrap Mass Spectrometer (MS) coupled to an Easy-nanoLC 1000 system with a flow rate of 300 nl/min. Peptides were eluted with 100 min with linear gradients from 2 to 35% acetonitrile (ACN) (85 min), from 35 to 85% ACN (5 min), and finally 85% (10 min) ACN in 0.1% formic acid (v/v %). Data-dependent acquisition mode was applied with a dynamic exclusion of 45 s, in every 3-s cycle, one full MS scan was collected with a scan range of 350 to 1500  $m/z$ , a resolution of 60,000 and the maximum injection time was 50 ms and auto-

matic gain control of 500,000. The MS2 scans were followed from the most intense parent ions. Ions were filtered with charge 2–5 with an isolation window of 1.5  $m/z$  in quadrupole isolation mode. Ions were fragmented using collision-induced dissociation with collision energy of 35%. Ion trap detection was used with normal scan range mode and rapid ion trap scan rate. Automatic gain was set to be 10,000 with a maximal injection time of 100 ms.

### Mass spectrometry analysis

Spectral analysis was conducted using Thermo Proteome Discoverer 2.0 (Thermo Scientific) and the Mascot Daemon search engine using a customized database containing kinesin sequences supplied for heterologous expression or the bovine proteome UniProt database for WT  $\alpha$ - and  $\beta$ -tubulins (UniProtKB ID P81947, Q2T9S0, Q3ZBU7, Q3MHM5, P81948, Q32KN8, Q2HJ86, Q3ZCJ7, Q6B856, Q2KJD0, Q2HJ81, and Q2HJB8). All analyses included dynamic oxidation of methionine (+15.9949  $m/z$ ) and static alkylation of cysteine (+57.0215  $m/z$ ; iodoacetamide alkylation). Photolabeled samples were run with the additional dynamic AziPm modification (+216.1996  $m/z$ ). A mass variation tolerance of 10 ppm for MS and 0.8 Da for MS/MS were used. Searches allowed for up to 3 missed trypsin cleavages with a false discovery rate of 0.01%. Samples were conducted in triplicate, and samples containing no photoaffinity ligand were treated similarly to control for false-positive detection of photoaffinity ligand modifications.

### Binding site prediction and docking

The X-ray crystal structures of kinesin motor domain without nucleotide (PDB ID 4LNU) (29) or with ADP-AlF<sub>4</sub><sup>-</sup> (PDB ID 4HNA) (30) in complex with tubulin were used for the propofol-binding site prediction and docking experiments. PyMOL (60) was used to remove the co-crystallized DARRPIN protein, ions, and crystallographic ligands as well as to mutate amino acid residues to align within with the K439 sequence. Prediction of the active site residues within the kinesin motor domain was analyzed using the CASTp web software (<http://cast.engr.uic.edu>)<sup>3</sup> (45) with a probe radius of 1 Å. Pockets with the greatest number of photolabeled residue sites lining the cavity and predicted have a sufficient volume (>200 Å<sup>3</sup>) were used as the basis for docking simulations using AutoDock Vina (46). Prior to docking, the structures were prepared using AutoDock Tools4 (61) with the addition of hydrogens and Kollman charges, and the merging of nonpolar hydrogens. Flexible residues were assigned based off the amino acid residues detected by CASTp that formed the predicted pocket and were defined using AutoDock Tools4. Molecular coordinates for propofol were downloaded from the ZINC small molecule library (62) using provided physical representations. The molecular coordinates for AziPm were generated using MarvinSketch version 16.3.28.0 and AutoDock Tools4 to generate Gasteiger charges and to merge nonpolar hydrogens. The maximum torsions were allowed for propofol and AziPm, respectively (*i.e.* ligands were fully flexible). Separate docking simulations using Auto-

<sup>3</sup> Please note that the JBC is not responsible for the long-term archiving and maintenance of this site or any other third party hosted site.



## Identification of inhibitory propofol site within kinesins

Dock Vina (46) were performed similar to as previously reported (44, 63) of the entire pocket predicted by CASTp. The grid box dimensions were  $24 \times 26 \times 20$  for the no nucleotide and  $28 \times 26 \times 26$  for the ADP- $\text{AlF}_4^-$  bound kinesin in complex with tubulin at 1-Å resolution. Images were prepared using PyMOL (60).

### Statistics

GraphPad Prism 7.0 was used for preparation of graphs and statistical analysis unless otherwise noted. All *p* values are reported in the tables and figure legends, as appropriate.

**Author contributions**—K. A. W., S. P. G., and R. G. E. conceptualization; K. A. W., S. G.-L., B. M. B., and N. V. B. data curation; K. A. W., S. G.-L., B. M. B., and S. P. G. formal analysis; K. A. W., S. G.-L., B. M. B., S. P. G., and R. G. E. investigation; K. A. W., S. G.-L., B. M. B., N. V. B., and R. G. E. methodology; K. A. W. and R. G. E. writing-original draft; K. A. W., S. G.-L., B. M. B., N. V. B., W. P. D., B. A. G., S. P. G., and R. G. E. writing-review and editing; B. M. B. validation; W. P. D., B. A. G., S. P. G., and R. G. E. resources; W. P. D., B. A. G., S. P. G., and R. G. E. funding acquisition; B. A. G. software; S. P. G. and R. G. E. project administration; R. G. E. supervision.

### References

1. Bentley, M., and Banker, G. (2016) The cellular mechanisms that maintain neuronal polarity. *Nat. Rev. Neurosci.* **17**, 611–622 [CrossRef Medline](#)
2. Hirokawa, N., Niwa, S., and Tanaka, Y. (2010) Molecular motors in neurons: transport mechanisms and roles in brain function, development, and disease. *Neuron* **68**, 610–638 [CrossRef Medline](#)
3. Maday, S., Twelvetrees, A. E., Moughamian, A. J., and Holzbaur, E. L. (2014) Axonal transport: cargo-specific mechanisms of motility and regulation. *Neuron* **84**, 292–309 [CrossRef Medline](#)
4. Hirokawa, N., Noda, Y., Tanaka, Y., and Niwa, S. (2009) Kinesin superfamily motor proteins and intracellular transport. *Nat. Rev. Mol. Cell Biol.* **10**, 682–696 [CrossRef Medline](#)
5. Miki, H., Setou, M., Kaneshiro, K., and Hirokawa, N. (2001) All kinesin superfamily protein, KIF, genes in mouse and human. *Proc. Natl. Acad. Sci. U.S.A.* **98**, 7004–7011 [CrossRef Medline](#)
6. Viancour, T. A., and Kreiter, N. A. (1993) Vesicular fast axonal transport rates in young and old rat axons. *Brain Res.* **628**, 209–217 [CrossRef Medline](#)
7. Kaether, C., Skehel, P., and Dotti, C. G. (2000) Axonal membrane proteins are transported in distinct carriers: a two-color video microscopy study in cultured hippocampal neurons. *Mol. Biol. Cell* **11**, 1213–1224 [CrossRef Medline](#)
8. Lasek, R. J., Garner, J. A., and Brady, S. T. (1984) Axonal transport of the cytoplasmic matrix. *J. Cell Biol.* **99**, 212s–221s [CrossRef Medline](#)
9. Paschal, B. M., and Vallee, R. B. (1987) Retrograde transport by the microtubule-associated protein MAP 1C. *Nature* **330**, 181–183 [CrossRef Medline](#)
10. Paschal, B. M., Shpetner, H. S., and Vallee, R. B. (1987) MAP 1C is a microtubule-activated ATPase which translocates microtubules *in vitro* and has dynein-like properties. *J. Cell Biol.* **105**, 1273–1282 [CrossRef Medline](#)
11. Fu, M., and Holzbaur, E. L. (2014) Integrated regulation of motor-driven organelle transport by scaffolding proteins. *Trends Cell Biol.* **24**, 564–574 [CrossRef Medline](#)
12. Verhey, K. J., Kaul, N., and Soppina, V. (2011) Kinesin assembly and movement in cells. *Annu. Rev. Biophys.* **40**, 267–288 [CrossRef Medline](#)
13. Kozielski, F., Sack, S., Marx, A., Thormählen, M., Schönbrunn, E., Biou, V., Thompson, A., Mandelkow, E. M., and Mandelkow, E. (1997) The crystal structure of dimeric kinesin and implications for microtubule-dependent motility. *Cell* **91**, 985–994 [CrossRef Medline](#)
14. Kull, F. J., Sablin, E. P., Lau, R., Fletterick, R. J., and Vale, R. D. (1996) Crystal structure of the kinesin motor domain reveals a structural similarity to myosin. *Nature* **380**, 550–555 [CrossRef Medline](#)
15. Aizawa, H., Sekine, Y., Takemura, R., Zhang, Z., Nangaku, M., and Hirokawa, N. (1992) Kinesin family in murine central nervous system. *J. Cell Biol.* **119**, 1287–1296 [CrossRef Medline](#)
16. Muresan, V., Abramson, T., Lyass, A., Winter, D., Porro, E., Hong, F., Chamberlin, N. L., and Schnapp, B. J. (1998) KIF3C and KIF3A form a novel neuronal heteromeric kinesin that associates with membrane vesicles. *Mol. Biol. Cell* **9**, 637–652 [CrossRef Medline](#)
17. Sardella, M., Navone, F., Rocchi, M., Rubartelli, A., Viggiano, L., Vignali, G., Consalez, G. G., Sitia, R., and Cabibbo, A. (1998) KIF3C, a novel member of the kinesin superfamily: sequence, expression, and mapping to human chromosome 2 at 2p23. *Genomics* **47**, 405–408 [CrossRef Medline](#)
18. Yamazaki, H., Nakata, T., Okada, Y., and Hirokawa, N. (1995) KIF3A/B: a heterodimeric kinesin superfamily protein that works as a microtubule plus end-directed motor for membrane organelle transport. *J. Cell Biol.* **130**, 1387–1399 [CrossRef Medline](#)
19. Yang, Z., and Goldstein, L. S. (1998) Characterization of the KIF3C neural kinesin-like motor from mouse. *Mol. Biol. Cell* **9**, 249–261 [CrossRef Medline](#)
20. Hua, W., Young, E. C., Fleming, M. L., and Gelles, J. (1997) Coupling of kinesin steps to ATP hydrolysis. *Nature* **388**, 390–393 [CrossRef Medline](#)
21. Schnitzer, M. J., and Block, S. M. (1997) Kinesin hydrolyses one ATP per 8-nm step. *Nature* **388**, 386–390 [CrossRef Medline](#)
22. Svoboda, K., Schmidt, C. F., Schnapp, B. J., and Block, S. M. (1993) Direct observation of kinesin stepping by optical trapping interferometry. *Nature* **365**, 721–727 [CrossRef Medline](#)
23. Asbury, C. L., Fehr, A. N., and Block, S. M. (2003) Kinesin moves by an asymmetric hand-over-hand mechanism. *Science* **302**, 2130–2134 [CrossRef Medline](#)
24. Kaseda, K., Higuchi, H., and Hirose, K. (2003) Alternate fast and slow stepping of a heterodimeric kinesin molecule. *Nat. Cell Biol.* **5**, 1079–1082 [CrossRef Medline](#)
25. Yildiz, A., Tomishige, M., Vale, R. D., and Selvin, P. R. (2004) Kinesin walks hand-over-hand. *Science* **303**, 676–678 [CrossRef Medline](#)
26. Bensel, B. M., Guzik-Lendrum, S., Masucci, E. M., Woll, K. A., Eckenhoff, R. G., and Gilbert, S. P. (2017) Common general anesthetic propofol impairs kinesin processivity. *Proc. Natl. Acad. Sci. U.S.A.* **144**, E4281–E4287 [Medline](#)
27. Friedman, E. B., Sun, Y., Moore, J. T., Hung, H.-T., Meng, Q. C., Perera, P., Joiner, W. J., Thomas, S. A., Eckenhoff, R. G., Sehgal, A., and Kelz, M. B. (2010) A conserved behavioral state barrier impedes transitions between anesthetic-induced unconsciousness and wakefulness: evidence for neural inertia. *PLoS ONE* **5**, e11903 [CrossRef Medline](#)
28. Hall, M. A., Xi, J., Lor, C., Dai, S., Pearce, R., Dailey, W. P., and Eckenhoff, R. G. (2010) m-Azipropropofol (AziPm) a photoactive analogue of the intravenous general anesthetic propofol. *J. Med. Chem.* **53**, 5667–5675 [CrossRef Medline](#)
29. Cao, L., Wang, W., Jiang, Q., Wang, C., Knossow, M., and Gigant, B. (2014) The structure of apo-kinesin bound to tubulin links the nucleotide cycle to movement. *Nat. Commun.* **5**, 5364 [CrossRef Medline](#)
30. Gigant, B., Wang, W., Dreier, B., Jiang, Q., Pecqueur, L., Plückthun, A., Wang, C., and Knossow, M. (2013) Structure of a kinesin-tubulin complex and implications for kinesin motility. *Nat. Struct. Mol. Biol.* **20**, 1001–1007 [CrossRef Medline](#)
31. Liu, D., Liu, X., Shang, Z., and Sindelar, C. V. (2017) Structural basis of cooperativity in kinesin revealed by 3D reconstruction of a two-head-bound state on microtubules. *Elife* 10.7554/eLife.24490
32. Rice, S., Lin, A. W., Safer, D., Hart, C. L., Naber, N., Carragher, B. O., Cain, S. M., Pechatnikova, E., Wilson-Kubalek, E. M., Whittaker, M., Pate, E., Cooke, R., Taylor, E. W., Milligan, R. A., and Vale, R. D. (1999) A structural change in the kinesin motor protein that drives motility. *Nature* **402**, 778–784 [CrossRef Medline](#)
33. Shang, Z., Zhou, K., Xu, C., Csencsits, R., Cochran, J. C., and Sindelar, C. V. (2014) High-resolution structures of kinesin on microtubules provide a basis for nucleotide-gated force-generation. *Elife* **3**, e04686 [Medline](#)

34. Hirokawa, N., Sato-Yoshitake, R., Kobayashi, N., Pfister, K. K., Bloom, G. S., and Brady, S. T. (1991) Kinesin associates with anterogradely transported membranous organelles *in vivo*. *J. Cell Biol.* **114**, 295–302 [CrossRef Medline](#)
35. Takeda, S., Yamazaki, H., Seog, D. H., Kanai, Y., Terada, S., and Hirokawa, N. (2000) Kinesin superfamily protein 3 (KIF3) motor transports fodrin-associating vesicles important for neurite building. *J. Cell Biol.* **148**, 1255–1265 [CrossRef Medline](#)
36. Castle, M. J., Perlson, E., Holzbaur, E. L., and Wolfe, J. H. (2014) Long-distance axonal transport of AAV9 is driven by dynein and kinesin-2 and is trafficked in a highly motile Rab7-positive compartment. *Mol. Ther.* **22**, 554–566 [CrossRef Medline](#)
37. Hendricks, A. G., Perlson, E., Ross, J. L., Schroeder, H. W., 3rd, Tokito, M., and Holzbaur, E. L. (2010) Motor coordination via a tug-of-war mechanism drives bidirectional vesicle transport. *Curr. Biol.* **20**, 697–702 [CrossRef Medline](#)
38. Block, S. M., Goldstein, L. S., and Schnapp, B. J. (1990) Bead movement by single kinesin molecules studied with optical tweezers. *Nature* **348**, 348–352 [CrossRef Medline](#)
39. Lasek, R. J., and Brady, S. T. (1985) Attachment of transported vesicles to microtubules in axoplasm is facilitated by AMP-PNP. *Nature* **316**, 645–647 [CrossRef Medline](#)
40. Vale, R. D., Reese, T. S., and Sheetz, M. P. (1985) Identification of a novel force-generating protein, kinesin, involved in microtubule-based motility. *Cell* **42**, 39–50 [CrossRef Medline](#)
41. Woll, K. A., Dailey, W. P., Brannigan, G., and Eckenhoff, R. G. (2016) Shedding light on anesthetic mechanisms: application of photoaffinity ligands. *Anesth. Analg.* **123**, 1253–1262 [CrossRef Medline](#)
42. Bayley, H. (1983) *Photogenerated Reagents in Biochemistry and Molecular Biology, Laboratory Techniques in Biochemistry and Molecular Biology*, Elsevier, New York [CrossRef](#)
43. Weiser, B. P., Woll, K. A., Dailey, W. P., and Eckenhoff, R. G. (2014) Mechanisms revealed through general anesthetic photolabeling. *Curr. Anesth. Rep.* **4**, 57–66 [CrossRef](#)
44. Jayakar, S. S., Zhou, X., Chiara, D. C., Dostalova, Z., Savechenkov, P. Y., Bruzik, K. S., Dailey, W. P., Miller, K. W., Eckenhoff, R. G., and Cohen, J. B. (2014) Multiple propofol binding sites in a  $\gamma$ -aminobutyric acid type A receptor (GABAAR) identified using a photoreactive propofol analog. *J. Biol. Chem.* **289**, 27456–27468 [CrossRef Medline](#)
45. Dundas, J., Ouyang, Z., Tseng, J., Binkowski, A., Turpaz, Y., and Liang, J. (2006) CASTp: computed atlas of surface topography of proteins with structural and topographical mapping of functionally annotated residues. *Nucleic Acids Res.* **34**, W116–8 [CrossRef Medline](#)
46. Trott, O., and Olson, A. J. (2010) AutoDock Vina: improving the speed and accuracy of docking with a new scoring function, efficient optimization, and multithreading. *J. Comput. Chem.* **31**, 455–461 [Medline](#)
47. Tischfield, M. A., Baris, H. N., Wu, C., Rudolph, G., Van Maldergem, L., He, W., Chan, W.-M., Andrews, C., Demer, J. L., Robertson, R. L., Mackey, D. A., Ruddle, J. B., Bird, T. D., Gottlob, I., Pieh, C., *et al.* (2010) Human TUBB3 mutations perturb microtubule dynamics, kinesin interactions, and axon guidance. *Cell* **140**, 74–87 [CrossRef Medline](#)
48. Tischfield, M. A., Cederquist, G. Y., Gupta, M. L., Jr., and Engle, E. C. (2011) Phenotypic spectrum of the tubulin-related disorders and functional implications of disease-causing mutations. *Curr. Opin. Genet. Dev.* **21**, 286–294 [CrossRef Medline](#)
49. Niwa, S., Takahashi, H., and Hirokawa, N. (2013)  $\beta$ -Tubulin mutations that cause severe neuropathies disrupt axonal transport. *EMBO J.* **32**, 1352–1364 [CrossRef Medline](#)
50. Minoura, I., Takazaki, H., Ayukawa, R., Saruta, C., Hachikubo, Y., Uchimura, S., Hida, T., Kamiguchi, H., Shimogori, T., and Muto, E. (2016) Reversal of axonal growth defects in an extraocular fibrosis model by engineering the kinesin-microtubule interface. *Nat. Commun.* **7**, 10058 [CrossRef Medline](#)
51. Ulaganathan, V., Talapatra, S. K., Rath, O., Pannifer, A., Hackney, D. D., and Kozielski, F. (2013) Structural insights into a unique inhibitor binding pocket in kinesin spindle protein. *J. Am. Chem. Soc.* **135**, 2263–2272 [CrossRef Medline](#)
52. Yan, Y., Sardana, V., Xu, B., Homnick, C., Halczenko, W., Buser, C. A., Schaber, M., Hartman, G. D., Huber, H. E., and Kuo, L. C. (2004) Inhibition of a mitotic motor protein: where, how, and conformational consequences. *J. Mol. Biol.* **335**, 547–554 [CrossRef Medline](#)
53. Wood, K. W., Lad, L., Luo, L., Qian, X., Knight, S. D., Nevins, N., Brejc, K., Sutton, D., Gilmartin, A. G., Chua, P. R., Desai, R., Schauer, S. P., McNulty, D. E., Annan, R. S., Belmont, L. D., *et al.* (2010) Antitumor activity of an allosteric inhibitor of centromere-associated protein-E. *Proc. Natl. Acad. Sci. U.S.A.* **107**, 5839–5844 [CrossRef Medline](#)
54. Olsen, R. W., and Li, G. D. (2011) GABA(A) receptors as molecular targets of general anesthetics: identification of binding sites provides clues to allosteric modulation. *Can. J. Anaesth.* **58**, 206–215 [CrossRef Medline](#)
55. Bryson, H. M., Fulton, B. R., and Faulds, D. (1995) Propofol- An update of its use in anesthesia and conscious sedation. *Drugs* **50**, 513–559 [CrossRef Medline](#)
56. Leite, L. F., Gomez, R. S., Fonseca, M. de C., Gomez, M. V., and Guatimosim, C. (2011) Effect of intravenous anesthetic propofol on synaptic vesicle exocytosis at the frog neuromuscular junction. *Acta Pharmacol. Sin.* **32**, 31–37 [CrossRef Medline](#)
57. Mintz, C. D., Smith, S. C., Barrett, K. M., and Benson, D. L. (2012) Anesthetics interfere with the polarization of developing cortical neurons. *J. Neurosurg. Anesth.* **24**, 368–375 [CrossRef](#)
58. Albracht, C. D., Rank, K. C., Obrzut, S., Rayment, I., and Gilbert, S. P. (2014) Kinesin-2 KIF3AB exhibits novel ATPase characteristics. *J. Biol. Chem.* **289**, 27836–27848 [CrossRef Medline](#)
59. Guzik-Lendrum, S., Rank, K. C., Bense, B. M., Taylor, K. C., Rayment, I., and Gilbert, S. P. (2015) Kinesin-2 KIF3AC and KIF3AB can drive long-range transport along microtubules. *Biophys. J.* **109**, 1472–1482 [CrossRef Medline](#)
60. Schrödinger, LLC. (2015) *The PyMOL Molecular Graphics System*, version 1.8, Schrödinger, LLC, New York
61. Morris, G. M., Huey, R., Lindstrom, W., Sanner, M. F., Belew, R. K., Goodsell, D. S., and Olson, A. J. (2009) AutoDock4 and AutoDockTools4: automated docking with selective receptor flexibility. *J. Comput. Chem.* **30**, 2785–2791 [CrossRef Medline](#)
62. Irwin, J. J., Sterling, T., Mysinger, M. M., Bolstad, E. S., and Coleman, R. G. (2012) ZINC: a free tool to discover chemistry for biology. *J. Chem. Inf. Model* **52**, 1757–1768 [CrossRef Medline](#)
63. Woll, K. A., Peng, W., Liang, Q., Zhi, L., Jacobs, J. A., Maciunas, L., Bhanu, N., Garcia, B. A., Covarrubias, M., Loll, P. J., Dailey, W. P., and Eckenhoff, R. G. (2017) Photoaffinity ligand for the inhalational anesthetic sevoflurane allows mechanistic insight into potassium channel modulation. *ACS Chem. Biol.* **12**, 1353–1362 [CrossRef Medline](#)